Synthesis of Co-Doped MoS$_2$ Monolayers with Enhanced Valley Splitting

Jiadong Zhou, Junhao Lin, Hunter Sims, Chongyun Jiang, Chunxiao Cong, John A. Brehm, Zhaowei Zhang, Lin Niu, Yu Chen, Yao Zhou, Yanlong Wang, Fucai Liu, Chao Zhu, Ting Yu, Kazu Suenaga, Rohan Mishra, Sokrates T. Pantelides, Zhen-Gang Zhu,* Weibo Gao,* Zheng Liu,* and Wu Zhou*

Internal magnetic moments induced by magnetic dopants in MoS$_2$ monolayers are shown to serve as a new means to engineer valley Zeeman splitting (VZS). Specifically, successful synthesis of monolayer MoS$_2$ doped with the magnetic element Co is reported, and the magnitude of the valley splitting is engineered by manipulating the dopant concentration. Valley splittings of 3.9, 5.2, and 6.15 meV at 7 T in Co-doped MoS$_2$ with Co concentrations of 0.8%, 1.7%, and 2.5%, respectively, are achieved as revealed by polarization-resolved photoluminescence (PL) spectroscopy. Atomic-resolution electron microscopy studies clearly identify the magnetic sites of Co substitution in the MoS$_2$ lattice, forming two distinct types of configurations, namely isolated single dopants and tridopant clusters. Density functional theory (DFT) and model calculations reveal that the observed enhanced VZS arises from an internal magnetic field induced by the tridopant clusters, which couples to the spin, atomic orbital, and valley magnetic moment of carriers from the conduction and valence bands. The present study demonstrates a new method to control the valley pseudospin via magnetic dopants in layered semiconducting materials, paving the way toward magneto-optical and spintronic devices.

Monolayer transition metal dichalcogenides (TMDCs) with broken inversion symmetry and direct bandgap offer the possibility to control their valley polarization for memory, logic, and quantum devices applications.[1–3] Valley Zeeman splitting has been experimentally observed in pristine MX$_2$ (M = W or Mo; X = S, Se, or Te) monolayers;[4–13] however, the achievable valley splitting and Landé *g*-factor in these pristine monolayers are relatively small. Theoretical studies predicted that a giant and tunable valley splitting can be obtained in monolayer MoTe$_2$ on a ferromagnetic EuO substrate due to the interfacial magnetic exchange field,[14] which has recently been confirmed experimentally using monolayer WSe$_2$ on ferromagnetic EuS and CrI$_3$ substrates.[15,16] In principle, internal magnetic moments induced by magnetic dopants in TMDC monolayers should also be able to engineer the valley splitting.

Dr. J. Zhou, Dr. L. Niu, Dr. F. Liu, Dr. C. Zhu, Prof. Z. Liu
School of Materials Science and Engineering
Nanyang Technological University
Singapore 639798, Singapore
E-mail: z.liu@ntu.edu.sg

Dr. J. Lin, Prof K. Suenaga
National Institute of Advanced Industrial Science
and Technology (AIST)
Tsukuba 305–8565, Japan

Dr. J. Lin
Department of Physics
Southern University of Science and Technology
Shenzhen 518055, China

Dr. H. Sims, Dr. J. A. Brehm, Prof. S. T. Pantelides
Department of Physics and Astronomy
Vanderbilt University
Nashville, TN 37235, USA

Dr. H. Sims, Dr. J. A. Brehm, Prof. S. T. Pantelides
Materials Science and Technology Division
Oak Ridge National Lab
Oak Ridge, TN 37831, USA

Dr. C. Jiang, Dr. C. Cong, Z. Zhang, Dr. Y. Chen, Dr. Y. Zhou,
Dr. Y. Wang, Prof. T. Yu, Prof. W. Gao
Division of Physics and Applied Physics
School of Physical and Mathematical Sciences
Nanyang Technological University
Singapore 637371, Singapore
E-mail: wbgao@ntu.edu.sg

Dr. C. Jiang
College of electronic information and optical engineering
Nankai University
Tianjin 300350, China

Dr. C. Cong
State Key Laboratory of ASIC & System
School of Information Science and Technology
Fudan University
Shanghai 200433, P. R. China

Dr. R. Mishra
Department of Mechanical Engineering and Materials Science
and Institute of Materials Science and Engineering
Washington University in St. Louis
St. Louis, MO 63130, USA

Prof. Z.-G. Zhu
School of Electronic
Electrical and Communication Engineering
University of Chinese Academy of Science
Beijing 100049, China
E-mail: zgzhu@ucas.ac.cn

ADVANCED
SCIENCE NEWS
www.advancedsciencenews.com

ADVANCED
MATERIALS
www.advmat.de

Theoretical studies have shown that local magnetism can be introduced in semiconducting MoS_2 via substitutional doping with magnetic elements, such as V, Cr, Mn, Fe, Co, or Ni.[17–20] The changes in the electronic and magnetic structures upon doping can subsequently affect the valley pseudospin. However, incorporating these magnetic dopants into monolayer MoS_2 lattice in a controllable manner remains challenging[21–23] and has hindered the systematic study of their influence on the valley pseudospin. Controlled synthesis of monolayer MoS_2 doped with specific magnetic elements is a desirable first step in order to explore the manipulation of valley pseudospin via internal magnetic moments.

In this work, we demonstrate the successful incorporation of a magnetic element (Co) into MoS_2 monolayers at various concentrations via chemical vapor deposition (CVD). The atomic configurations and chemical identities of the Co dopants were analyzed via annular dark-field (ADF) imaging and electron energy loss spectroscopy (EELS) at the single-atom level on an aberration-corrected low-voltage scanning transmission electron microscope (STEM). Both single dopants and tridopant triangular clusters were observed in Co-doped MoS_2. The presence of the tridopant clusters gives rise to enhanced valley Zeeman splitting in the Co-doped monolayer MoS_2, with values a few times larger than those for pristine TMDCs. More importantly, the magnitude of the valley Zeeman splitting can be tuned via controlling the concentration of Co dopants. Density functional theory (DFT) calculations confirm that the thermodynamic stability of Co dopants is enhanced by the formation of these triangular Co clusters surrounding a central sulfur vacancy. Further, these calculations reveal ferromagnetic coupling within the tridopant clusters, leading to an internal magnetic field in the Co-doped semiconducting MoS_2 monolayers. Finally, at doping levels of a few percent, it is shown that the internal magnetic field plays an essential role in the giant enhanced valley Zeeman splitting. The overlapping of the dopant and carrier wave functions is the microscopic mechanism that underlies this observation.

The growth setup for doped MoS_2 monolayers is shown in Figure S1 (Supporting Information), and detailed information on the synthesis can be found in the Experimental Section. **Figure 1**a shows the optical image of a Co-doped MoS_2

Prof. Z.-G. Zhu, Prof. W. Zhou
CAS Center for Excellence in Topological Quantum Computation
University of Chinese Academy of Sciences
Beijing 100049, China
E-mail: wuzhou@ucas.ac.cn

Prof. Z. Liu
Centre for Micro-/Nano-electronics (NOVITAS)
School of Electrical & Electronic Engineering
Nanyang Technological University
50 Nanyang Avenue, Singapore 639798, Singapore

Prof. Z. Liu
CINTRA CNRS/NTU/THALES
UMI 3288
Research Techno Plaza
50 Nanyang Drive, Border X Block, Level 6, Singapore 637553, Singapore

Prof. W. Zhou
School of Physical Sciences and CAS Key Laboratory of Vacuum Sciences
University of Chinese Academy of Sciences
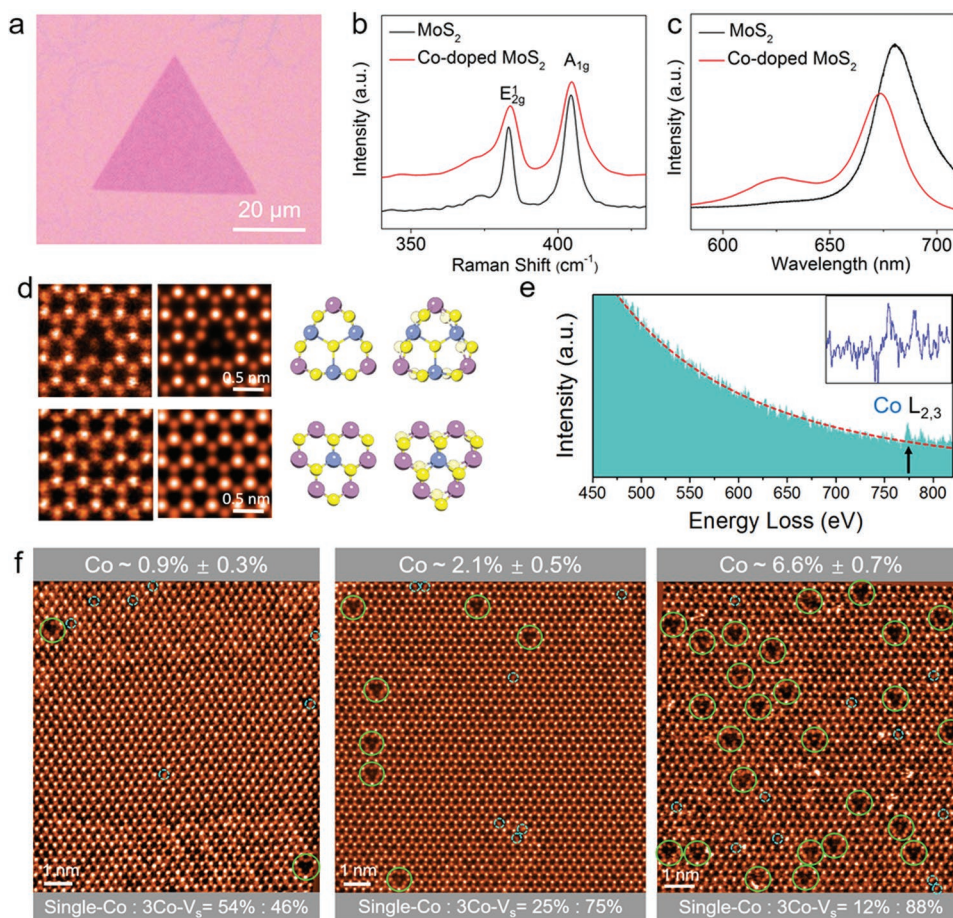Beijing 100049, China

monolayer sample. Most of the doped MoS_2 monolayer domains show the characteristic triangular shape frequently observed in CVD grown MoS_2, an indication of their high crystallinity. The optical image of MoS_2 on a large wafer is shown in Figure S2 in the Supporting Information. The Co-doped MoS_2 with different dopant concentrations can be achieved by controlling the mole ratio of the precursors, as presented in the Experimental Section. The averaged doping concentration of the magnetic elements was analyzed via X-ray photoelectron spectroscopy (XPS) combined with STEM results. The peak positions of Co2*p* in the XPS spectra as shown in Figure S3 (Supporting Information) demonstrate the formation of chemical bonding between the dopant atoms and sulfur in the MoS_2 lattice, which is different from the CoMoS phase (see details in Figure S3 in the Supporting Information). Atomic force microscopy (AFM) analysis confirms that the as-synthesized Co-doped MoS_2 domain is indeed monolayer, as shown in Figure S4 in the Supporting Information. The Raman spectra of the Co-doped MoS_2 and pristine MoS_2 monolayers are shown in Figure 1b. All the doped samples display the characteristic A_g mode around $\approx$401 cm^{-1} and the E_g mode around $\approx$381 cm^{-1} in the Raman spectra, indicating that the Co-doped MoS_2 preserves similar lattice feature as the pristine MoS_2 crystals. Photoluminescence (PL) spectra in Figure 1c confirm the monolayer feature of the doped-MoS_2 samples. The corresponding Raman and PL mapping are shown in Figure S2 (Supporting Information), demonstrating the uniformity of Co-doped MoS_2.

We used atomic-resolution STEM–ADF imaging and EELS analysis to confirm the incorporation of magnetic dopants into the MoS_2 lattice and simultaneously identify their local atomic configurations. Theoretical studies have found that the magnetic elements can substitute Mo atoms in the MoS_2 lattice,[20,24] forming a single substitutional defect. Figure 1d shows the STEM images of Co dopants in MoS_2 lattice. The Mo (brighter) atoms and S (dimmer) column can be clearly distinguished in the MoS_2 lattice, owing to the atomic number (*Z*) contrast in the STEM images. Due to the smaller atomic number of Co, they show similar contrast levels to that of the disulfur columns and lower than that of the Mo atoms in the STEM–ADF images. In other words, the dimmer contrast at the Mo sites is most likely arising from Co dopants. However, note that under sulfur-rich CVD growth conditions, disulfur (S_2) can occupy Mo sites forming antisite defects,[25] which generate similar STEM–ADF image contrast as observed here. In order to unambiguously confirm the incorporation of the magnetic dopants into the MoS_2 lattice, we further used atomic-scale STEM–EELS analysis to pinpoint the chemical identities of the low-contrast metal sites. EELS spectra acquired from the individual metal sites (Figure 1e) clearly show the characteristic $L_{2,3}$ edges of the Co dopants, confirming the formation of substitutional magnetic dopants into the MoS_2 lattice. Based on the STEM–ADF images, we found two distinct configurations of Co dopants in the MoS_2 lattice, namely the isolated single dopants and the tridopant clusters with a central S vacancy (V_S). Simulated STEM–ADF images along with the corresponding atomic structural models for the two types of dopant configurations are shown next to the experimental images, showing an excellent agreement.

To further validate the tunability of the Co dopant concentration in MoS_2 monolayer, we statistically examined the Co

ADVANCED
SCIENCE NEWS
www.advancedsciencenews.com

ADVANCED
MATERIALS
www.advmat.de

Figure 1. Structural characterizations of Co-doped MoS_2. a) Optical image of Co-doped MoS_2, with a doping concentration of ≈1%. b,c) Raman and PL spectra of the corresponding Co-doped MoS_2. The spectra of pristine MoS_2 monolayer are provided for comparison. The presence of the A_g mode around ≈401 cm^{-1} and the E_g mode around ≈381 cm^{-1} indicate that the MoS_2 structure is preserved despite the small dopant concentration. It can be clearly seen that two PL peaks of Co-doped MoS_2 at 625 and 675 nm are observed. The PL peak located at 625 nm at room temperature originates from the B exciton. d) Experimental atom-resolved ADF-STEM and simulated STEM images along with the corresponding structural models of the two types of dopant configurations found in Co-doped MoS_2. The images reveal the presence of isolated single dopants and tridopant clusters substituted in the Mo sites in Co-doped MoS_2. The slightly tilted atomic models on the right are shown for direct visualization of the disulfur columns. e) The corresponding single-atom EELS analysis of the dopants shown in inset (d). The red dashed lines indicate the background signal. The insets are the enlarged background subtracted EELS of Co $L_{2,3}$ edges. f) Typical ADF-STEM images of Co-doped MoS_2 monolayers with different dopant concentrations. The single isolated Co dopant and tridopant are indicated by light blue and green circles, respectively. The Co concentration is estimated by statistical analysis of random regions sampled across the same flake where the presented ADF–STEM images were taken. The relative population ratio of the two dopant configurations is listed below the corresponding images. The appearance of the tridopant cluster becomes dominant as the dopant concentration increases.

concentration in Co-doped MoS_2 monolayers with different designed dopant concentrations. We sampled each flake in random regions and mapped out the Co dopants by their lower intensity, part of which were verified by corresponding single atom EELS measurements. Figure 1f shows representative 10 nm × 10 nm regions of three Co-doped MoS_2 monolayers with different Co concentration. The Co concentration is estimated by atom counting of the Co dopants, which shows an average concentration of 0.9% ± 0.3%, 2.1% ± 0.5%, and 6.6% ± 0.7% (from left to right), demonstrating the flexible tunability of Co dopant concentration in MoS_2 lattice using our CVD method. The relative population ratio of the isolated single dopants (indicated by the light blue circles) and tridopant clusters with a central S vacancy (indicated by the green circles) are also provided in Figure 1f. It was found that at low doping concentration

(Figure 1f, left), Co atoms have almost equal probability to form either dopant configurations, while the tridopant cluster with a central S vacancy becomes the dominant configuration as the average Co concentration increases, suggesting that the excessive Co atoms tend to aggregate when substituting the metal sites in the MoS_2 lattice at high concentration.

DFT calculations on the formation and binding energies of the two types of Co dopant configurations further support the experimental observations. We find that it is energetically favorable for transition-metal impurities substituting Mo to form three-atom complexes with a central S vacancy, with a formation energy of 0.2 eV for a three-dopant cluster as compared to 2 eV for an isolated single dopant (Figure S5, Supporting Information). Figure S5 also shows the formation energy of three-atom clusters (per dopant atom) without a central S

vacancy for different elements. Even under S-rich growth conditions, the three-atom clusters of Co gain energy by losing the central S atom. The gain in energy upon the formation of a three-atom cluster, i.e., their binding energy, is further shown in Figure S5 in the Supporting Information for Co dopants. The binding energy is very strong for Co (>4 eV). Overall, the DFT calculations suggest that Co dopants show preference to form a three-atom cluster with a central V_S that helps to reduce their oxidation state from +4 as in the perfect MoS_2 lattice. These results are in excellent agreement with the experimental observations, which show a strong preference for forming triangle clusters with a central V_S as the Co concentration increases.

We have further investigated the local magnetic moments due to magnetic interaction within the three-dopant-atom clusters in Co-doped MoS_2. We find that the spins of the three dopant atoms in the cluster are ferromagnetically coupled to each other as shown in the spin-isosurface plots in Figure S6 in the Supporting Information. Each $3Co_{Mo}+1V_S$ cluster has a magnetic moment of 1 μ_B. We also find that the spin of the neighboring S atoms couples antiferromagnetically to the dopant spins, which suggests an antiferromagnetic superexchange interaction between the dopants and the chalcogens. The delocalized nature of the S 3p states, when combined with the antiferromagnetic interaction between the spins of the sulfur atoms and the triatom Co clusters, can be expected to result in the effective long-range ferromagnetic coupling between triatom clusters that are a few Ångströms apart, especially under an applied magnetic field. Such a superexchange interaction has been theoretically proposed to result in the long-range ferromagnetic coupling between spins of 3d transition metals dopants in MoS_2 and other oxides.[26,27]

The tunability of Co concentration in Co-doped MoS_2 monolayers provides an excellent platform to explore the influence of the internal magnetic moments on the valley pseudospin. We studied the valley splitting in Co-doped MoS_2 using polarization-resolved PL in a magnetic field perpendicular to the 2D plane from −7 to 7 T at a temperature of 4 K. Specifically, we only considered the exciton in monolayer MoS_2. The temperature-dependent and laser-power-dependent PL in Co-doped MoS_2 (Figures S7 and S8, Supporting Information) confirm that the emission originates from excitons rather than defects.[28,29]

The lattice structure and valley magnetic moments of MoS_2 are shown in Figure S9 in the Supporting Information. **Figure 2**a,c displays the normalized PL spectra for the neutral exciton peak in Co-doped MoS_2 with the dopant concentration of 0.8%, at 7, 0, and −7 T, respectively. At a high field of 7 T (−7 T) (Figure 2a,c), the PL spectrum from the +K valley exciton is different to that from the −K valley exciton, indicating valley Zeeman splitting between σ^+ and σ^-. The splitting reaches 3.9 meV at a high field of 7 T (−7 T). In contrast, no splitting is observed at zero field. The zero valley Zeeman splitting at 0 T indicates that time-reversal symmetry is preserved and the magnetic moments of the Co dopant atoms are randomly oriented. At high magnetic fields, on the other hand, the dopant-atom magnetic moments become ordered, which breaks time invariance and leads to the observed splitting, as shown in Figure 2a,c. The normalized PL spectra at different fields from −5 to 5 T are presented in Figure S10 in the Supporting Information.

In order to further study the ferromagnetic dopant influence on the valley Zeeman splitting in MoS_2, we also measured the polarized PL under the same conditions in Co-doped MoS_2 monolayers with dopant concentrations of 1.7% and 2.5%. The corresponding results are shown in Figure 2d–f,g–i. It can be clearly seen that the valley Zeeman splitting increases as the dopant concentration increases. The splitting reaches 5.2 and 6.15 meV at high magnetic field of 7 T for dopant concentrations of 1.7% and 2.5%, respectively. These results suggest that the Co dopants can effectively tune the valley splitting due to their ferromagnetic coupling to the MoS_2 valley structure. The corresponding valley-exciton Zeeman splitting of MoS_2 with different dopant concentrations as a function of magnetic field from −7 to 7 T is shown in **Figure 3**a, yielding positive slopes of 0.56, 0.71, and 0.87 meV T^{-1}, respectively, for dopant concentrations of 0.8%, 1.7%, and 2.5%. More importantly, the Landé g-factors calculated from the valley Zeeman splitting are 9.64, 12.22, and 14.99 for the Co-doped MoS_2 with increasing Co concentration, which are significantly larger than previously reported results in other pristine TMDC monolayers, as shown in Table S1 in the Supporting Information.[4–9,15,30]

In order to obtain a better understanding of the source of the enhanced valley g-factor in the Co-doped MoS_2, we carried out both DFT calculations and a model study. For pristine MoS_2, an applied magnetic field B couples to three different magnetic moments: spin, atomic orbital, and valley pseudospin, each of which produces a Zeeman-like splitting in the band energies (**Figure 4**a). Excitations from circularly polarized light conserve spin, whereby the spin-Zeeman splitting has no net effect on the optical gap. The conduction-band-edge states carry no atomic-orbital angular momentum ($m_l = 0$), while the valence band edge states do ($m_l = 2$ at −K and −2 at K), leading to a band shift $|\Delta_a| = 2\mu_B B$. Finally, the valley pseudospin contributes a term given by $\Delta_v = \alpha_c\,\tau_z\mu_B B$ or $\alpha_v\tau_z\mu_B B$ for the conduction or valence bands,[7] where τ_z is the valley pseudospin. The total valley splitting reads

$$\Delta E_0\,(B) = E_K^0\,(B) - E_{-K}^0\,(B) = 2(2-\Delta\alpha)\mu_B B \tag{1}$$

where the index "0" refers to the pristine material without doping. The induced band edge shifts are schematically shown in Figure 4a.

For the case of Co doping, atomic-scale STEM analysis has identified both substitutional single dopant and tridopant configurations. For the isolated single dopant where a Co atom replaces one Mo atom in the lattice, there are five electrons with up spins occupying the 4d orbitals of one Mo atom, while seven electrons on the 3d orbitals of a Co atom, leaving three up spins occupying $m_l = 2$, 1, and 0, respectively. Therefore, these substitutional single Co dopants contribute to the localized bonding-reconstruction of the partial states at the valence band edge, but may not lead to an enhancement of the valley splitting as compared to that of pristine MoS_2 (see Section S2 in the Supporting Information for a more detailed discussion).

For the tridopant case (dominant in our experiment), the three spins are coupled ferromagnetically around a vacancy (Figure S6, Supporting Information) so that a local magnetic moment is formed. The carriers' spins have exchange interactions with these local magnetic moments, leading to an internal
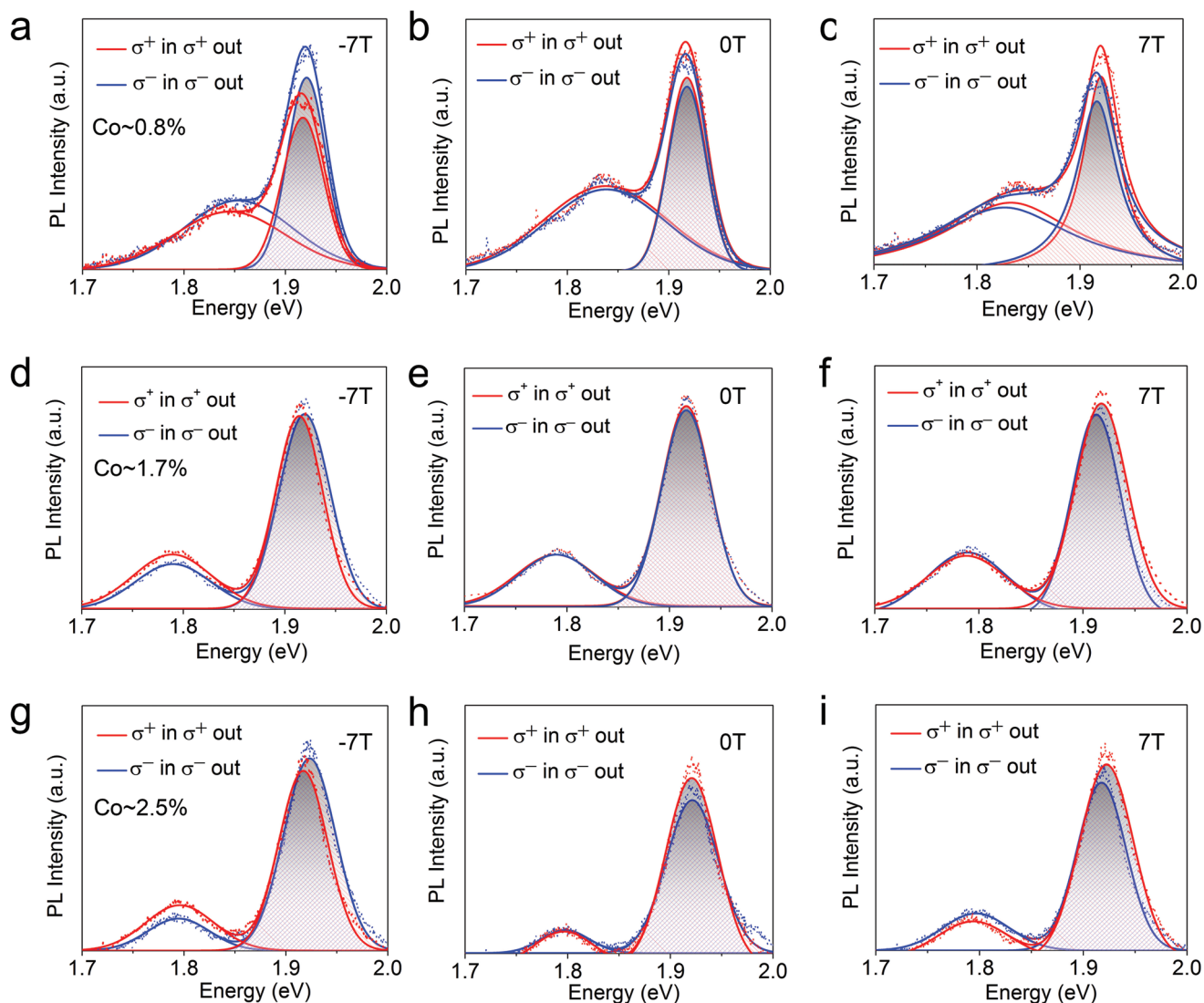
Figure 2. Valley Zeeman splitting in Co-doped MoS$_2$ with different dopant concentration. a–i) Polarization-resolved valley-exciton PL of Co-doped MoS$_2$ at −7, 0, and 7 T, respectively, with Co concentrations of 0.8% (a–c), 1.7% (d–f), and 2.5% (g–i). The red and blue curves represent PL spectra when excited and detected with a single helicity, corresponding to the K and −K valleys, respectively. Dots: raw data; curves: Gaussian fitted results.

magnetic field B_{in} under a virtual-crystal approximation.[31] We will show that the presence of the B_{in} explains the giant enhanced valley splitting in our experiment (see Section S2 in the Supporting Information for a more detailed discussion). The B_{in}-field interacts not only with the spin degree of freedom, but also with atomic orbital moments and the valley magnetic moments. In contrast to an applied B-field, the B_{in}-field couples to carriers in the conduction and valence bands nonequally so that the B_{in}-field spin-Zeeman splitting has net effect on the optical gap. This nonequal coupling to conduction and valence bands holds for the coupling of the B_{in}-field to the atomic orbital and valley magnetic moments as well. The total valley splitting is included in

$$\Delta E_{inter} = 2\mu_B \langle S_z \rangle \left\{ -x \frac{(N_0\delta)}{\mu_B} + 2x \frac{(N_0 \langle J_{AV} \rangle)}{\mu_B} + x \left[-\frac{\alpha_C N_0 \langle J_{VC} \rangle}{\mu_B} + \frac{\alpha_V N_0 \langle J_{VV} \rangle}{\mu_B} \right] \right\}$$

(2)

where x represents dopant concentration, $\langle S_z \rangle$ indicates the internal magnetic field expressed by an average over local magnetic moments of tridopants, $N_0\delta = N_0\beta - N_0\alpha$, $\alpha = \langle KV|(r)|KV \rangle$, $\beta = \langle KC|J(r)|KC \rangle$, $|KV(KC)\rangle$ indicate the states for the valence (conduction) band in the K valley, and $J(r) = \sum_R J(r-R)$ describes the s–d exchange interaction between spins and local magnetic moments, $\langle J_{AV} \rangle = \langle KV|J_{AV}|KV \rangle$, $\langle J_{VC} \rangle = \langle KC|J_{VC}|KC \rangle$, $\langle J_{VV} \rangle = \langle KV|J_{VV}|KV \rangle$. Basically, these parameters can be determined by fitting the experimental data in terms of these formulas. To express the physical picture more clearly, we rewrite Equation (2) as

$$\Delta E_{inter} = g_s \mu_B B_{in} + g_a \mu_B B_{in} + g_v \mu_B B_{in}$$

(3)

where $g_s \mu_B B_{in} = -2x(N_0\delta)\langle S_z \rangle$, $g_a \mu_B B_{in} = 4x(N_0 \langle J_{AV} \rangle)\langle S_z \rangle$, $g_v \mu_B B_{in} = 2x[-\alpha_C N_0 \langle J_{VC} \rangle + \alpha_V N_0 \langle J_{VV} \rangle]\langle S_z \rangle$. The band-edge-shifts induced by the B_{in}-field are schematically shown in Figure 4b.
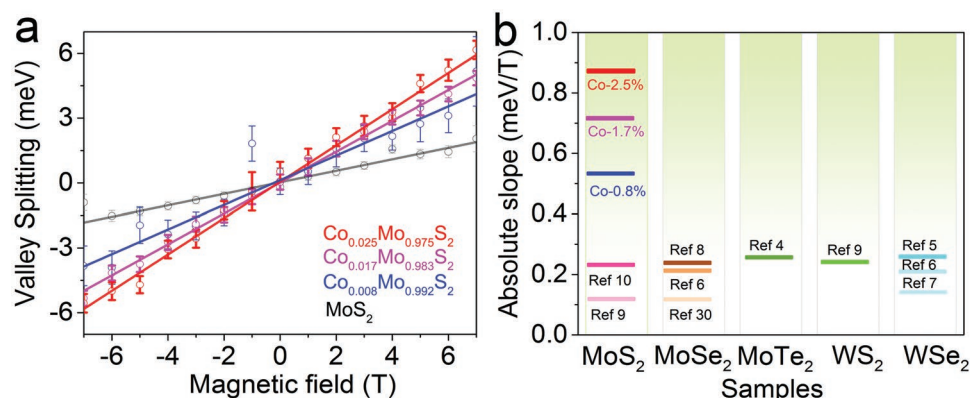
Figure 3. Comparison of the magnitude of valley splitting in Co-doped MoS_2 with different dopant concentrations. a) Zeeman valley splitting as a function of the magnetic field in Co-doped MoS_2 with different dopant concentrations from −7 to 7 T. The pristine MoS_2, Co concentrations of 0.8% (blue), 1.7% (magenta), and 2.5% (red) correspond to a slope of 0.26, 0.56, 0.72, and 0.87 meV T^{-1}, respectively. b) Comparisons of the Zeeman valley splitting slops in different samples in the current literature. The Zeeman valley splitting in Co-doped MoS_2 is larger than reported values in pristine MoS_2,[9,10] $MoSe_2$,[6,8,30] WS_2,[9] pristine WSe_2[5–7] and pristine $MoTe_2$.[4] It can be clearly seen that the Zeeman valley splitting increases as the dopant concentration increases in Co-doped MoS_2, indicating that the Co doping can effectively tune the Zeeman valley in MoS_2.

For a rough estimation, we assume $N_0\delta = N_0\langle J_{AV}\rangle = N_0\langle J_{VC}\rangle = N_0\langle J_{VV}\rangle$ and the experimental data at 7 T, e.g., $x = 0.8\%$, $k = 0.56$ meV $T^{-1} = 9.675$ μ_B; $x = 1.7\%$, $k = 0.72$ meV $T^{-1} = 12.440$ μ_B; $x = 2.5\%$, $k = 0.87$ meV $T^{-1} = 15.031$ μ_B, and arrive at $N_0\delta \approx -0.5$ eV, which is comparable to those found in dilute magnetic semiconductors.[32]

In summary, we have successfully synthesized MoS_2 monolayers doped with magnetic Co atoms via CVD method. Atomic-scale electron microscopy studies confirm that the Co atoms substitute the Mo sites within the lattice, where isolated single dopants and tridopant clusters with a central sulfur vacancy are formed, as confirmed by DFT calculations. We find that an internal magnetic field B_{in} is formed by the tridopants, which couples to the spin, atomic orbital, and valley magnetic moment of carriers from conduction and valence bands. The coupling of spin with the B_{in} field is distinct to that for an external magnetic field B. The B_{in}-field affects the PL shift, while the external B-field does not. The internal magnetic field results in a giant enhancement of the valley splitting, stemming from the inherent overlap of carrier and impurity wave functions. Our results demonstrate a possible way to tune the valley pseudospin in TMDCs by magnetic atom doping. The large valley Zeeman splitting makes Co-doped MoS_2 a promising candidate for magneto-optical and spintronic device applications.
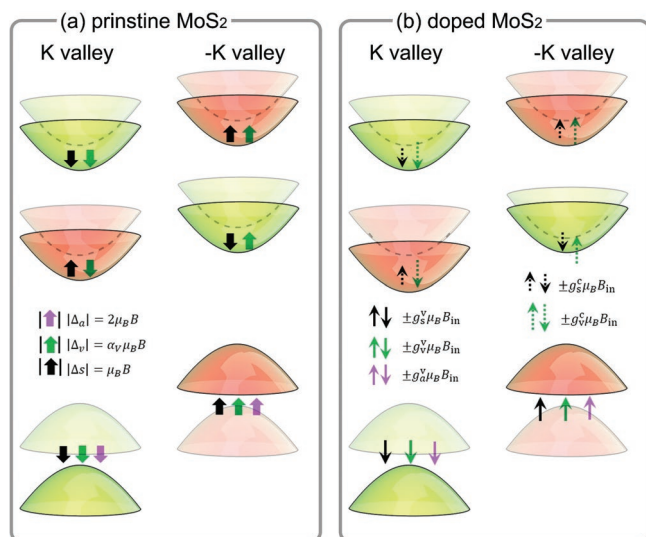

Figure 4. a) A comparison is shown for pristine MoS_2. In principle, the internal magnetic field in doped MoS_2 couples to the conduction band and valence band nonequally, which is distinct to the external magnetic field. Therefore, the shifts of the optical gap are related to the relative difference of the effects on the conduction and valence bands. The superscripts "c" and "v" in the g-factors represent the conduction and valence bands, respectively. The subscripts "s," "a," and "v" in the g-factors refer to spin, atomic orbital moment, and valley magnetic moment, respectively. b) Schematic illustration of the Zeeman-like splitting induced by the internal magnetic field for doped MoS_2.

Experimental Section

Synthesis of MoS_2 and Co-Doped MoS_2: Pure MoS_2 and doped MoS_2 were synthesized by CVD method using MoO_3 and sulfur (Sigma) as the reaction sources. $CoCl_2$ was used as the dopant source. The pure MoS_2 and doped-MoS_2 were synthesized in quartz tubes (1-inch diameter) under temperature ranging from 700 to 750 °C. The setup for the growth is shown in Figure S1 in the Supporting Information. Specifically, for the pure MoS_2, Ar flow of 80 sccm was used as the carrier gas and a silicon boat contained 10 mg MoO_3 was put in the center of the tube. The SiO_2/Si substrate is placed on the boat with the surface downside. Another silicon boat containing 0.5 g S powder was located on the upstream. The temperature ramped up to 750 °C in 15 min, and was kept at the reaction temperature for about 5 min to 10 min. Then the furnace was cooled down to room temperature gradually. For the Co-doped MoS_2, the boat containing mixed powder of $CoCl_2$ and MoO_3 (mole ratio of 1: 99, 2: 98, 3: 97, and 6 for Co-doped MoS_2) was put in the center of the tube. The reaction condition was similar to the synthesis of pure MoS_2, except that it used mixed Ar/H_2 with a flow of 80/5 sccm as the carrier gas.

Raman and PL Characterization: Room temperature: Raman and PL measurements with an excitation laser of 532 nm were performed using a WITEC alpha 300R Confocal Raman system. Before Raman

characterization, the system was calibrated with the Raman peak of Si at 520 cm^{-1}. The laser powers were less than 1 mW to avoid overheating of the samples.

PL measurements at 4 K: A homemade fiber-based confocal microscope was used for polarization-resolved PL spectroscopy. The wavelength of the excitation is 532 nm. The excitation power is ≈270 µW within a spot of ≈1 µm in diameter. Polarizers and quarter wave plates were installed to generate and detect circular polarization. The PL emission was collected into a spectrometer (Andor Shamrock 500i) with a CCD camera via a multimode fiber for spectroscopy recording. The sample was placed in a magneto-cryostat in a Faraday geometry and cooled down to 4 K. The magnetic field up to 7 T was perpendicular to the sample plane. Note that all the spectra for all magnetic fields have been fitted using Gaussian functions. The peak positions from the Gaussian fitting were used to calculate the valley splitting, and the errors were taken as the error bars in Figure 3a.

STEM Characterization: The TEM samples were prepared with a poly (methyl methacrylate) (PMMA) assisted method. A layer of PMMA of about 1 µm thick was spin-coated on the wafer with doped MoS_2 samples deposited and then baked at 180 °C for 3 min. Afterward, the wafer was immersed in NaOH solution (1 M) to etch the SiO_2 layer overnight. After lift-off, the doped MoS_2 sample was transferred into DI water for several cycles to wash away the residual contaminants, and then it was fished by a TEM grid (Quantifoil Mo grid). The as-transferred specimen was dried naturally in the ambient environment, and then dropped into acetone overnight to wash away the PMMA coating layers. The STEM analysis was performed on an aberration-corrected JEOL 2100F with a cold field-emission gun and an aberration corrector (the DELTA-corrector), operating at 60 kV. All STEM experiments were performed at room temperature.

DFT Calculations: DFT calculations were performed using a plane-wave basis set with cut-off energy of 450 eV and the projector-augmented-wave (PAW)[33] method as implemented within the Vienna Ab initio Simulation Package (VASP).[34,35] Exchange and correlation effects were described within the Generalized Gradient Approximation (GGA) in the Perdew–Burke–Ernzerhof (PBE) parameterization.[36] A 5 × 5 × 1 supercell of the MoS_2 primitive cell was used with ≈20 Å vacuum to simulate monolayer MoS_2. To check the convergence of the results with respect to supercell size, some calculations were repeated using a larger 7 × 7 × 1 supercells. A 3 × 3 × 1 Γ-centered Monkhorst–Pack (MP) grid[37] was used for structural relaxations where only the atomic positions were optimized, and (5 × 5 × 1) k-points mesh was used for the electronic calculation. The formation energy (E_f) of the dopant structure in a 25 formula unit MoS_2 supercell, for instance, a transition metal-substituted MoS_2 without or with a sulfur vacancy: $TM_xMo_{25-x}S_{50-y}$, is described as[38]

$$E_f = \frac{E(TM_xMo_{25-x}S_{50-y}) + x(\mu_{Mo} - \mu_{MT}) + y\mu_s - 25E(MoS_2)}{x} \quad (4)$$

where, $E(TM_xMo_{25-x}S_{50-y})$ is the DFT total energy of the dopant structure, $E(MoS_2)$ is the total energy of one formula unit of MoS_2 and μ_i is the chemical potential of element i. The formation energy as defined in Equation (3) is expressed per TM dopant atom. Experimentally, as the transition metals substitute Mo atoms, the growth conditions were considered to be Mo-poor or S-rich. Hence, μ_S was defined as half the energy of a S_2 molecule as obtained by DFT and $\mu_{Mo} = E(MoS_2) - 2\mu_S$. μ_{TM} is further defined as the difference in energy between the most stable form of the transition metal sulfide (TM_xS_y) as obtained from the Materials Project Database[39] and μ_S. The most stable sulfides for V, Cr, Mn, Fe, Co, and Ni are V_3S_4, Cr_2S_3, MnS_2 (hexagonal form), FeS_2, Co_3S_4, and Ni_3S_4, respectively.

To investigate the tendency of a transition metal dopant to form a triatom cluster, the binding energy E_b was used, which is defined as

$$E_b = 3E(TM_1Mo_{24}S_{50}) - E(TM_3Mo_{22}S_{50}) - 50E(MoS_2) \quad (5)$$

In Equation (4), a positive binding energy suggests a tendency to form a triatom cluster.

Supporting Information

Acknowledgements

Conflict of Interest

The authors declare no conflict of interest.

Keywords

[1] J. Lee, K. F. Mak, J. Shan, *Nat. Nanotechnol.* **2016**, *11*, 421.

[2] H. T. Yuan, M. S. Bahramy, K. Morimoto, S. F. Wu, K. Nomura, B. J. Yang, H. Shimotani, R. Suzuki, M. Toh, C. Kloc, X. D. Xu, R. Arita, N. Nagaosa, Y. Iwasa, *Nat. Phys.* **2013**, *9*, 563.

[3] Y. Ye, J. Xiao, H. L. Wang, Z. L. Ye, H. Y. Zhu, M. Zhao, Y. Wang, J. H. Zhao, X. B. Yin, X. Zhang, *Nat. Nanotechnol.* **2016**, *11*, 597.

[4] A. Arora, R. Schmidt, R. Schneider, M. R. Molas, I. Breslavetz, M. Potemski, R. Bratschitsch, *Nano Lett.* **2016**, *16*, 3624.

[5] A. Srivastava, M. Sidler, A. V. Allain, D. S. Lembke, A. Kis, A. Imamoglu, *Nat. Phys.* **2015**, *11*, 141.

[6] G. Wang, L. Bouet, M. M. Glazov, T. Amand, E. L. Ivchenko, E. Palleau, X. Marie, B. Urbaszek, *2D Mater.* **2015**, *2*, 034002.

[7] G. Aivazian, Z. R. Gong, A. M. Jones, R. L. Chu, J. Yan, D. G. Mandrus, C. W. Zhang, D. Cobden, W. Yao, X. Xu, *Nat. Phys.* **2015**, *11*, 148.

[8] Y. L. Li, J. Ludwig, T. Low, A. Chernikov, X. Cui, G. Arefe, Y. D. Kim, A. M. van der Zande, A. Rigosi, H. M. Hill, S. H. Kim, J. Hone, Z. Q. Li, D. Smirnov, T. F. Heinz, *Phys. Rev. Lett.* **2014**, *113*, 148.

[9] A. V. Stier, K. M. McCreary, B. T. Jonker, J. Kono, S. A. Crooker, *Nat. Commun.* **2016**, *7*, 10643.

[10] F. Cadiz, E. Courtade, C. Robert, G. Wang, Y. Shen, H. Cai, T. Taniguchi, K. Watanabe, H. Carrere, D. Lagarde, M. Manca, T. Amand, P. Renucci, S. Tongay, X. Marie, B. Urbaszek, *Phys. Rev. X* **2017**, *7*, 021026.

[11] A. A. Mitioglu, P. Plochooka, A. G. del Aguila, P. C. M. Christianen, G. Deligeorgis, S. Anghel, L. Kulyuk, D. K. Maude, *Nano Lett.* **2015**, *15*, 4387.

[12] A. A. Mitioglu, K. Galkowski, A. Surrente, L. Klopotowski, D. Dumcenco, A. Kis, D. K. Maude, P. Plochocka, *Phys. Rev. B* **2016**, *93*, 165412.

[13] A. V. Stier, N. P. Wilson, G. Clark, X. D. Xu, S. A. Crooker, *Nano Lett.* **2016**, *16*, 7054.

[14] Q. Y. Zhang, S. Y. A. Yang, W. B. Mi, Y. C. Cheng, U. Schwingenschlogl, *Adv. Mater.* **2016**, *28*, 959.

[15] T. N. Chuan Zhao, P. Zhao, Y. Cheng, P. Zhang, F. Sun, P. Taheri, J. Wang, Y. Yang, T. Scrace, K. Kang, S. Yang, G.-x. Miao, R. Sabirianov, G. Kioseoglou, A. Petrou, H. Zeng, *Nat. Nanotechnol.* **2017**, *12*, 757.

[16] D. Zhong, K. L. Seyler, X. Y. Linpeng, R. Cheng, N. Sivadas, B. Huang, E. Schmidgall, T. Taniguchi, K. Watanabe, M. A. McGuire, W. Yao, D. Xiao, K. M. C. Fu, X. D. Xu, *Sci. Adv.* **2017**, *3*, e1603113.

[17] W. B. Xu, P. Li, S. S. Li, B. J. Huang, C. W. Zhang, P. J. Wang, *Phys. E* **2015**, *73*, 83.

[18] J. S. Qi, X. Li, X. F. Chen, K. G. Hu, *J. Phys.: Condens. Mater.* **2014**, *26*, 256003.

[19] X. L. Fan, Y. R. An, W. J. Guo, *Nanoscale Res. Lett.* **2016**, *11*, 154.

[20] R. Mishra, W. Zhou, S. J. Pennycook, S. T. Pantelides, J. C. Idrobo, *Phys. Rev. B* **2013**, *88*, 144409.

[21] K. H. Zhang, S. M. Feng, J. J. Wang, A. Azcatl, N. Lu, R. Addou, N. Wang, C. J. Zhou, J. Lerach, V. Bojan, M. J. Kim, L. Q. Chen, R. M. Wallace, M. Terrones, J. Zhu, J. A. Robinson, *Nano Lett.* **2015**, *15*, 6586.

[22] B. Li, L. Huang, M. Z. Zhong, N. J. Huo, Y. T. Li, S. X. Yang, C. Fan, J. H. Yang, W. P. Hu, Z. M. Wei, J. B. Li, *ACS Nano* **2015**, *9*, 1257.

[23] A. W. Robertson, Y. C. Lin, S. S. Wang, H. Sawada, C. S. Allen, Q. Chen, S. Lee, G. D. Lee, J. Lee, S. Han, E. Yoon, A. I. Kirkland, H. Kim, K. Suenaga, J. H. Warner, *ACS Nano* **2016**, *10*, 10227.

[24] A. Ramasubramaniam, D. Naveh, *Phys. Rev. B* **2013**, *87*, 195201.

[25] W. Zhou, X. L. Zou, S. Najmaei, Z. Liu, Y. M. Shi, J. Kong, J. Lou, P. M. Ajayan, B. I. Yakobson, J. C. Idrobo, *Nano Lett.* **2013**, *13*, 2615.

[26] A. N. Andriotis, M. Menon, *Phys. Rev. B* **2013**, *87*, 155309.

[27] A. N. Andriotis, M. Menon, *Phys. Rev. B* **2014**, *90*, 125304.

[28] Y. M. He, G. Clark, J. R. Schaibley, Y. He, M. C. Chen, Y. J. Wei, X. Ding, Q. Zhang, W. Yao, X. D. Xu, C. Y. Lu, J. W. Pan, *Nat. Nanotechnol.* **2015**, *10*, 497.

[29] A. Srivastava, M. Sidler, A. V. Allain, D. S. Lembke, A. Kis, A. Imamoglu, *Nat. Nanotechnol.* **2015**, *10*, 491.

[30] D. MacNeill, C. Heikes, K. F. Mak, Z. Anderson, A. Kormanyos, V. Zolyomi, J. Park, D. C. Ralph, *Phys. Rev. Lett.* **2015**, *114*, 037401.

[31] J. Sinova, *Int. J. Mod. Phys. B* **2004**, *18*, 1083.

[32] J. K. Furdyna, *J. Appl. Phys.* **1988**, *64*, R29.

[33] P. E. Blochl, *Phys. Rev. B* **1994**, *50*, 17953.

[34] G. Kresse, J. Hafner, *Phys. Rev. B* **1993**, *47*, 558.

[35] G. Kresse, J. Furthmuller, *Phys. Rev. B* **1996**, *54*, 11169.

[36] J. P. Perdew, K. Burke, M. Ernzerhof, *Phys. Rev. Lett.* **1996**, *77*, 3865.

[37] H. J. Monkhorst, J. D. Pack, *Phys. Rev. B* **1976**, *13*, 5188.

[38] S. B. Zhang, J. E. Northrup, *Phys. Rev. Lett.* **1991**, *67*, 2339.

[39] A. Jain, S. P. Ong, G. Hautier, W. Chen, W. D. Richards, S. Dacek, S. Cholia, D. Gunter, D. Skinner, G. Ceder, K. A. Persson, *APL Mater.* **2013**, *1*, 011002.